International Journal of Heat and Fluid Flow 44 (2013) 293–300

Contents lists available at SciVerse ScienceDirect

International Journal of Heat and Fluid Flow

journal homepage: www.elsevier.com/locate/ijhff

LES of the adverse-pressure gradient turbulent boundary layer

M. Inoue [a,*], D.I. Pullin [a], Z. Harun [b], I. Marusic [b]

[a] Graduate Aerospace Laboratories, California Institute of Technology, Pasadena, CA 91125, USA
[b] Department of Mechanical Engineering, University of Melbourne, Parkville, Victoria 3010, Australia

ARTICLE INFO

Article history:
Received 7 July 2012
Received in revised form 30 March 2013
Accepted 23 June 2013
Available online 27 July 2013

Keywords:
Adverse pressure gradient
Turbulent boundary layer
Wall-model LES

ABSTRACT

We describe large-eddy simulations (LES) of the flat-plate turbulent boundary layer in the presence of an adverse pressure gradient. The stretched-vortex subgrid-scale model is used in the domain of the flow coupled to a wall model that explicitly accounts for the presence of a finite pressure gradient. The LES are designed to match recent experiments conducted at the University of Melbourne wind tunnel where a plate section with zero pressure gradient is followed by section with constant adverse pressure gradient. First, LES are described at Reynolds numbers based on the local free-stream velocity and the local momentum thickness in the range 6560–13,900 chosen to match the experimental conditions. This is followed by a discussion of further LES at Reynolds numbers at approximately 10 times and 100 times these values, which are well out of range of present day direct numerical simulation and wall-resolved LES. For the lower Reynolds number runs, mean velocity profiles, one-point turbulent statistics of the velocity fluctuations, skin friction and the Clauser and acceleration parameters along the streamwise, adverse pressure-gradient domain are compared to the experimental measurements. For the full range of LES, the relationship of the skin-friction coefficient, in the form of the ratio of the local free-stream velocity to the local friction velocity, to both Reynolds number and the Clauser parameter is explored. At large Reynolds numbers, a region of collapse is found that is well described by a simple log-like empirical relationship over two orders of magnitude. This is expected to be useful for constant adverse-pressure gradient flows. It is concluded that the present adverse pressure gradient boundary layers are far from an equilibrium state.

© 2013 Elsevier Inc. All rights reserved.

1. Introduction

There is a growing need for reliable, accurate LES techniques and subgrid-scale (SGS) models suitable for real-world flows. The boundary layer over aerospace vehicles, for both the inner flow or outer flow, usually exhibits complex behavior at high Reynolds numbers. In spite of recent advances in computational capabilities, highly accurate simulations, for example, of separated flow on the wings of airplanes or for flow through turbine blades in jet engines has not been achieved. When such simulations become possible at reasonable computational cost, engineers in industry will be able to investigate other critical problems that are at the moment accessible only by costly physical experiments. As a step toward this, we presently consider the LES of the adverse-pressure gradient flat-plate turbulent boundary layer at both moderate and quite large Reynolds numbers. The LES uses a combination of a wall model and an interior SGS model (Chung and Pullin, 2009; Inoue and Pullin, 2011), which are both entirely local in character including the incorporation of local pressure gradients, and therefore should be applicable to adverse-pressure-gradient turbulent boundary layers (APGTBL).

Although there are some established features in APGTBL such as the amplified wake of the mean velocity profile and the increasing turbulence intensity in the outer region, the difficulty in APGTBL research is the wide range of parameters that have to be considered such as the upstream history, the local pressure gradient, and whether the flow should be in some defined form of equilibrium. Commonly, a constant nondimensional pressure gradient parameter (Clauser, 1956),

$$\beta = \frac{\delta^*}{\tau_w}\frac{dP}{dx}, \tag{1}$$

where δ^* is the displacement thickness, τ_w is the wall shear stress and dP/dx is the pressure gradient, has been taken as a condition for "equilibrium" layers whose velocity profiles, Clauser (1956) proposed, are identical when plotted in a velocity defect form at each cross section. Mellor and Gibson (1966) and Bradshaw (1967) have suggested that an approximate equilibrium flow is obtained when the variation of local free-stream velocity has the form of a power-law relation in the streamwise direction. That is to say, a practically constant β results if the outer-edge velocity is chosen

* Corresponding author. Tel.: +1 (626)395 4747.
E-mail address: minoue@caltech.edu (M. Inoue).

0142-727X/$ - see front matter © 2013 Elsevier Inc. All rights reserved.
http://dx.doi.org/10.1016/j.ijheatfluidflow.2013.06.011

as $U_\infty \sim (x - x_0)^m$, where x_0 is a virtual origin, and m is a constant power.

Skote et al. (1998) summarized previous theoretical and experimental work on selfsimilar turbulent boundary layer flows under adverse-pressure gradients. Those works seem to reach a consensus that separation occurs for $-0.25 < m < -0.20$ with a shape factor of about 2. Also Schofield (1981) concluded that no selfsimilar solution can be achieved for $m < -0.3$ and only one selfsimilar solution exists for $m > -0.23$. Skote et al. (1998) reviewed relations between m and β using the assumption of infinite Reynolds number and the use of specific velocity and length scales. Including the works mentioned above, this class of equilibrium APGTBL have been studied by both numerical simulations (e.g., Henkes et al., 1997; Skote et al., 1998; Hickel and Adams, 2008; Lee and Sung, 2008; Lee et al., 2010) and experiments (e.g., Skåre and Krogstad, 1994; Nagano et al., 1998).

There are several other parameters that characterize APGTBL as discussed by Perry and Marusic (1995), Marusic and Perry (1995), and Perry et al. (2002), such as a skin friction parameter (or S-factor), the Coles' wake factor Π and a nonequilibrium parameter ξ, which is a function of a streamwise derivative of Π, the S-factor and the boundary layer thickness. Yet another class of "quasi-equilibrium" layers were postulated by Perry et al. (1994), which has selfsimilarity in both velocity and shear stress profiles, with Π being constant or allowed to vary in the streamwise direction but this variation is sufficiently slow. Under this condition, we have a selfsimilar velocity defect distribution implying a selfsimilar shear stress distribution. It should be noted that the above discussion, however, is based on the assumption that a universal logarithmic law exists. Nagib and Chauhan (2008) argued that this may not be suitable for the APGTBL since it has been observed by several researchers that the value of Kármán constant κ shows some sensitivity to the pressure gradient and that there seems to be a shift of the mean velocity profile from the log-law (e.g., Nagano et al., 1998; Nickels, 2004; Lee and Sung, 2008). As a result, depending on the log-law chosen, the wake factor Π can vary.

Monty et al. (2011) performed a parametric study of the behavior of the APGTBL and suggested that β is useful for characterizing the flow observing the good collapse in flow statistics with constant β. The effect of three parameters were investigated: a friction Reynolds number Re_τ, pressure gradient parameter β and an acceleration parameter

$$K = \frac{\nu}{U_\infty^2}\frac{dU_\infty}{dx}, \tag{2}$$

where U_∞ is the local free-stream velocity and ν is the kinematic viscosity.

Many important features of the APGTBL are well understood through extensive studies on "equilibrium" flows over the past decades. Compared with other canonical turbulence flows; pipe, channel and the zero-pressure-gradient turbulent boundary layer (ZPGTBL), however, the present state knowledge of the APGTBL is sparse (Marusic and Perry, 1995) and perhaps insufficient to draw conclusions on their general behaviors including the probably broad class of nonequilibrium APGTBLs. The latter remain to be investigated. There have been few attempts at LES of the flat-plate APGTBL flow. Hickel and Adams (2008) apply an implicit LES method to an APGTBL flow at Reynolds number $Re_\theta = \theta U_\infty/\nu$ based on the momentum thickness θ and the local free-stream velocity U_∞ up to $Re_\theta = 5100$. They utilize a wall-resolved technique that is able to capture large-scale separation but is useful only at moderate Re_θ.

Presently, we aim first to reproduce, using LES, the experimental setting of Monty et al. (2011) with a constant adverse pressure gradient, the simplest class of pressure distributions also seen in other canonical flows. This is followed by an extension of the LES to substantially larger Reynolds numbers. In Section 2, an account is given of the problem setting including matching the experimental pressure distribution. The numerical implementation of the present LES for the APGTBL over a range of Reynolds numbers is presented in Section 3, followed by results and discussion in Section 4 before the conclusions in Section 5.

2. Problem setting

We attempt to reproduce the experimental setup of an open-return blower wind tunnel, whose details can be found in Marusic and Perry (1995), Harun et al. (2010), and Monty et al. (2011). In the experiment, the pressure gradient was adjusted by the height of the flexible test section ceiling. The area of the tunnel cross-section increases nominally exponentially to maintain a constant pressure gradient. The flexible ceiling was configured so that a zero-pressure gradient is maintained until $x = 3$ m followed by an constant adverse-pressure gradient section thereafter until $x = 6.7$ m. Fig. 1 shows the coefficient of pressure C_p,

$$C_p = \frac{p - p_{\text{inlet}}}{\frac{1}{2}\rho U_{\text{inlet}}^2} = 1 - \left(\frac{U_\infty}{U_{\text{inlet}}}\right)^2, \tag{3}$$

along the streamwise direction in the tunnel and indicates five locations where streamwise velocities were measured by hot-wire anemometry, $x_1 = 2.90$ m, $x_2 = 3.50$ m, $x_3 = 4.00$ m, $x_4 = 4.46$ m and $x_5 = 4.78$ m. When applying the pressure boundary condition at the top in LES, a smooth function representation of C_p is used to avoid discontinuities. Table 1 shows experimental results at each location.

3. Simulation details

3.1. LES and LES wall model

Chung and Pullin (2009) developed an LES approach for near-wall flows based on combining the stretched-vortex SGS model with a wall model based on Dirichlet boundary conditions. First, an analytic integration of the local streamwise momentum equation across a constant-thickness, wall-adjacent layer together with local inner-scaling applied to the unsteady term produces an ordinary-differential equation (ODE) at each point on the wall for the wall-normal, mean velocity gradient $\eta(x, y, t)_w \equiv \partial\tilde{u}/\partial z$ where (x, y, z) are streamwise, spanwise and wall-normal co-ordinates respectively. The ODE contains both turbulent and viscous transport terms, the former supplied by the outer LES at or near the first wall-normal grid point, in addition to the local, instantaneous

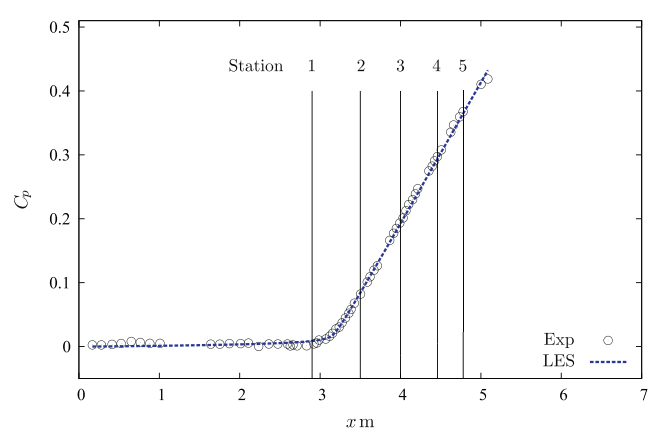

Fig. 1. Profile of coefficient of pressure C_p: Experimental measurements (Monty et al., 2011) and a smoothed profile used in LES.

Table 1
Experimental parameters for hot-wire anemometry at five measurement locations. The free-stream velocity at the inlet (x = 0 m) is U_{inlet} = 15.9 m/s.

Station	x (m)	U_∞ (m/s)	Re_τ	Re_θ	δ (m)	θ (m)
1	2.90	15.68	2330	6560	0.061	0.0064
2	3.50	15.12	2670	8570	0.076	0.0085
3	4.00	14.43	2380	8590	0.076	0.0095
4	4.46	13.43	2500	10,500	0.090	0.0122
5	4.78	12.89	2500	11,630	0.102	0.0143

pressure gradient term. It therefore allows dynamic calculation of the wall friction velocity $u_\tau^2 = \nu\eta(x,y,t)_w$ at every wall grid point. Further, the stretched vortex SGS model is used within a near-wall region where it is assumed that the subgrid vortex elements represent attached vortices in the presence of the wall with assumed scaling linearly proportional to distance from the wall. The wall model then provides a slip-velocity boundary condition at a raised virtual wall at $z = h_0$ as

$$\tilde{u}(h_0^+) = u_\tau\left(\frac{1}{\mathscr{K}_1}\log\left(\frac{h_0^+}{h_v^+}\right) + B\right), \quad B = h_v^+ - \frac{\log h_v^+}{\mathscr{K}_1}, \tag{4a}$$

$$\mathscr{K}_1(x,y,t) = \frac{\gamma_{\text{II}}K^{1/2}}{2\,(-T_{xz}/u_\tau)}. \tag{4b}$$

In (4a), $\mathscr{K}_1(x,y,t)$ is a parameter that is essentially a Kármán-like "constant" and T_{ij} is the subgrid stress tensor. These quantities are both calculated dynamically in the LES. The "mixing" parameter $\gamma_{\text{II}} = \sqrt{2}/\pi$, which is presently taken as constant, is obtained using Townsend's structure parameter (Chung and Pullin, 2009), $h_v^+ = 10.23$ is an empirical parameter that appears as an integration constant in obtaining Eq. (4a) and K is the local SGS kinetic energy. The local friction velocity u_τ is obtained from the numerical solution of the ODE while $\mathscr{K}_1(x,y,t)$ is provided by the LES. This provides information sufficient for the use of (4b) to provide a slip-velocity boundary condition, $\tilde{u}(h_0^+)$ at $z = h_0$, for the outer-flow LES. The filtered continuity equation provides the boundary condition for $\tilde{v}$ at $z = h_0$, and we take $\tilde{w} = 0$. This combination of outer-flow LES and a structure-based wall model has been applied to the LES of channel flow at Re_τ up to 2×10^7 Chung and Pullin (2009), and also to LES of the ZPGTBL at Re_θ up to $O(10^{12})$ Inoue and Pullin (2011). Further details on the LES methodology and the numerical scheme can be found in those papers and the references therein and only a short description will be provided here for the purpose of completness.

3.2. Numerical method and boundary conditions

The generically filtered nondimensional incompressible Navier–Stokes equations are

$$\frac{\partial\tilde{u}_i}{\partial t} + \frac{\partial\tilde{u}_i\tilde{u}_j}{\partial x_j} = -\frac{\partial\tilde{p}}{\partial x_i} + \frac{1}{Re_0}\frac{\partial^2\tilde{u}_i}{\partial x_j^2} - \frac{\partial T_{ij}}{\partial x_j}, \quad \frac{\partial\tilde{u}_i}{\partial x_i} = 0, \tag{5}$$

where $\tilde{u}_i$ is the filtered velocity, $T_{ij} = \widetilde{u_iu_j} - \tilde{u}_i\tilde{u}_j = \widetilde{\tilde{u}_i\tilde{u}_j} + \widetilde{u_i'\tilde{u}_j} + \widetilde{u_i'u_j'}$ is the subgrid stress tensor. $Re_0 = U_0\delta_0/\nu$ is the Reynolds number with U_0 and δ_0 is the free-stream velocity and the 99% boundary layer thickness at the inlet of the domain, respectively. ν is the kinematic viscosity and p is pressure divided by density. The fractional-step method (Perot, 1993) is used to solve the governing equations with the low-storage third-order semi-implicit Runge–Kutta method of Spalart et al. (1991) for temporal discretization. The viscous terms in the wall-normal direction are treated implicitly presently and the nonlinear and wall-parallel viscous terms are treated explicitly. The time-step size dt is dynamically adapted to satisfy a Courant–Friedrichs–Lewy (CFL) number be unity. Explicit, fourth-order finite differences on a staggered grid are used to approximate (x, z)-derivatives, while a pseudospectral method is utilized for y-derivatives. The Poisson solver employs fast cosine transform in streamwise direction, fast Fourier transforms in the spanwise direction, and the symmetric septa-diagonal matrix solver provided by LAPACK is used in the wall-normal direction. The Poisson equation is solved at every Runge-Kutta substep.

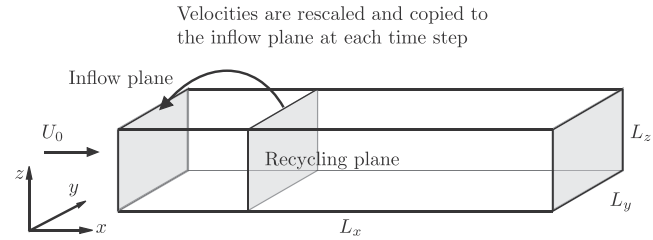

Fig. 2. A schematic of the computational domain showing the recycling region. The mirroring method (Jewkes et al., 2011) is employed in addition to the inflow generation scheme of Lund et al. (1998).

Conservation of kinetic energy in the inviscid limit is achieved by the numerical scheme with the use of staggered grids (Morinishi et al., 1998). The convective terms are calculated using a fully conservative skew-symmetric form. Nonlinear terms are treated using a pseudospectral method with a p_1th-order Fourier exponential filter in y-direction, which mimics the 2/3 rule, in order to prevent aliasing errors (Gottlieb and Shu, 1997; Chung and Pullin, 2009).

See Fig. 2 for the schematic of the computational domain. The boundary condition in the y-direction is periodic. For generating realistic inflow boundary conditions, we use the recycling method of Lund et al. (1998) combined with the mirroring method proposed by Jewkes et al. (2011). Briefly the velocity data at a downstream location (x_{ref}), referred to as the "recycling plane", is rescaled to account for the growth of the thickness of the boundary layer in the x-direction. It is then reintroduced at the inlet of the computational domain. The boundary conditions at the top of the domain are

$$P_\infty(x) = f(x) \quad \text{and} \quad \frac{\partial u}{\partial z} = \frac{\partial v}{\partial z} = 0. \tag{6}$$

Along with the top of the domain, the non-zero pressure gradient is specified at the outflow plane to reproduce the experimental pressure distribution $f(x)$. The velocity at the outflow are estimated by a convective boundary condition,

$$\frac{\partial\tilde{u}_i}{\partial t} + U_c(z)\frac{\partial\tilde{u}_i}{\partial x} = 0, \tag{7}$$

where $U_c(z)$ is the local mean streamwise velocity at the exit. It should be noted that the boundary conditions for the wall-normal velocity at the top and the streamwise velocity at outflow are not required in principal. When the pressure boundary condition is specified, boundary-normal velocities follow directly from the projection step, so that mass is conserved inside the computational domain. The issues on the pressure boundary condition was discussed in detail in Simens (2008) with respect to mass conservation and solving Helmholtz equations for pressure in the context of the fractional step method. No artificial damping or sponge zone is used here.

3.3. LES performed

In total the results of six different LES are reported in detail presently, which are summarized in Table 2. Case D1 was designed to match experimental conditions reported in Section 2 based on Re_θ = 6560 at $x_{1,\text{exp}}$ = 2.90 m in the experiment. Then the same

Table 2
Simulation parameters: $Re_0 = U_0\delta_0/\nu$; U_0 and δ_0 is the free-stream velocity and the 99% boundary layer thickness at the inlet of the domain, respectively. $\Delta_x = \Delta_y = 3\Delta_z$. $h_0 = 0.18\Delta_z$. x_{ref}, LES = 0.2 L_x, where x_{ref}, LES is the location where a velocity data is taken and rescaled for inflow velocities.

Case	Re_0	L_x/δ_0	L_y/δ_0	L_z/δ_0	N_x	N_y	N_z	h_0/δ_0(%)
D1	4.58×10^4	72	6	4	768	64	128	5.6e−3
D2	7.18×10^4	72	6	4	768	64	128	5.6e−3
D3	1.54×10^5	72	6	4	768	64	128	5.6e−3
D4	5.61×10^5	72	6	4	768	64	128	5.6e−3
D5	1.86×10^6	72	6	4	768	64	128	5.6e−3
D6	6.51×10^6	72	6	4	768	64	128	5.6e−3

pressure distribution is used for the other cases. The LES equations are normalized by using the free-stream velocity and the boundary layer thickness at the inflow plane, U_0 and δ_0, respectively. Typically an individual LES is done by fixing a nominal Reynolds number $Re_0 = U_0\delta_0/\nu$, so that the resulting Re_θ at $x_{1,\text{LES}}$ is close to the expected value. LES have been performed at resolutions $(N_x, N_y, N_z) = (768, 64, 128)$, the grid is uniform and $\Delta_x = \Delta_y = 3\Delta_z$ throughout the simulation domain without stretching in the wall-normal direction. The raised wall is at $h_0 = 0.18\,\Delta_z$ for all LES.

LES were performed in a domain $(L_x/\delta_0, L_y/\delta_0, L_z/\delta_0) = (72, 6, 4)$. The domain size in the streamwise direction is designed to be sufficiently long to cover the range between x_1 and x_5. Also the adverse-pressure gradient starts at $x_{1,\text{LES}} = 0.35L_x$ in the computational domain in order to allow a sufficiently long streamwise length from the inlet to obtain an equilibrium ZPGTBL on which the inflow generation scheme of Lund et al. (1998) is based. The location of the recycling plane is set at $x_{\text{ref,LES}} = 0.2L_x$ to avoid the effect of adverse-pressure gradient.

In case D1, our lowest Reynolds number case, the height of the raised "virtual" wall, $z = h_0$, where the wall-model provides the slip streamwise velocity, resides below the log-region, typically $h_0^+ < 10.23$. Therefore the log-like relationship used for the slip velocity used at larger Reynolds number (Chung and Pullin, 2009) is replaced with a linear profile

$$\widetilde{u^+}|_{h_0} = u_\tau h_0^+, \tag{8}$$

obtained by assuming the instantaneous streamwise velocity follows the linear relationship with inner-scaling within the viscous sublayer. The change from the log to the linear profile is dynamic and does not affect the operation of the ODE for wall-shear stress.

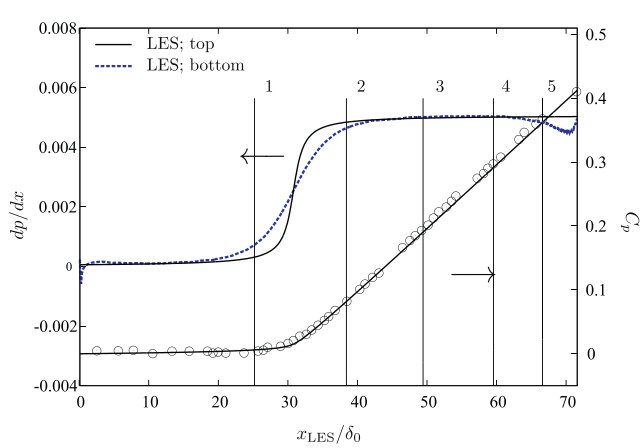

Fig. 3. Profile of coefficient of pressure C_p and the resulting pressure gradient distribution dp/dx in LES. Solid line; at top of the domain, dashed-line; at the first grid point from the virtual wall. ∘: Experimental measurements of C_p at corresponding streamwise locations (Monty et al., 2011).

4. Results and discussion

All results shown presently are obtained as spanwise/time averages. Fig. 3 shows profiles of the pressure coefficient C_p and the mean pressure gradient dp/dx in case D1. It is observed that the LES reproduces the C_p profile from the measurement at corresponding streamwise locations. The length scale is matched using the momentum thickness θ at station 1. Two pressure-gradient profiles are shown: one is the mean pressure gradient imposed at the top of the domain ($z = L_z$) and the other is at the first grid point from the virtual wall ($z = h_0 + \Delta_z/2$). The pressure gradient at the top is essentially prescribed by the pressure boundary condition. The profile at $z = h_0 + \Delta_z/2$ indicates the pressure gradient deviates from that at the top ($z = L_z$) toward the end of the domain. Aside from the fact that the mean pressure distribution at the bottom is the nonlinear response of the flow (Hickel and Adams, 2008), the deviation can also be attributed to the effect of the outflow boundary conditions. Other choices of $U_c(z)$ in Eq. (7) are the bulk velocity at the end of the domain, the local instantaneous velocity. Each choice gives a unique profile in the deviation (not shown) however the study of the outflow boundary condition is beyond the scope of the present work.

The increase in the pressure gradient at $x_{\text{LES}} \approx 30\delta_0$ is not as sharp as that at the top boundary. Similar profiles were observed for all the other LES cases (not shown). It is observed that the effect of non-zero-pressure gradient propagates upstream as far as 10 boundary layer thickness at the bottom of the domain. It should be noted that the recycling plane is located at $x_{\text{ref,LES}} \approx 14.4\delta_0$ where the pressure gradient is sufficiently small.

4.1. APG parameters

Fig. 4 show profiles of the Clauser pressure-gradient parameter β, the acceleration parameter K and the normalized pressure gradient $(dp/dx)^+ \equiv \nu(dp/dx)/(u_\tau^3)$ along the streamwise direction in cases D1, D4, and D6. Results for cases D2, D3 and D5 follow the trend shown here but are omitted for clarity. The excellent agreement of the accelerfation parameter K confirms that the boundary conditions reproduce the experiment correctly. Those parameters related to the streamwise pressure gradient show non-zero values even at the ZPG stretch of the domain, but they are sufficiently small to conclude that the flow is under zero-pressure gradient. See Wu and Moin (2009), for example, for the pressure gradient inside the DNS of transitional ZPGTBL. Albeit a slight difference up to 10%, the nondimensional pressure gradient, indicated by β shows a reasonably good collapse between the three LES cases. This indicates that the ratio of the pressure gradient acting across an effective face area of the layer δ^*, to the wall shear stress τ_w was kept almost constant over the range of Reynolds number. Note that the pressure distribution prescribed at the domain top is the same for all the cases, as is the resulting local free-stream velocity. Therefore the displacements of the profiles of K between cases are due to the difference in kinematic viscosity ν for each case. The S-factor, $S \equiv U_\infty/u_\tau$ shows a clear increase with both Reynolds number and β; also see Fig. 9. We remark that S is related to the local skin-friction coefficient as $C_f = 2/S^2$.

Table 3 provides LES results of case D1 and their corresponding experimental results at five locations along the streamwise direction. The acceleration parameter K shows good agreement with the experiments, indicating the adverse-pressure gradient boundary conditions at the domain top results in the decreasing local free-stream velocity sufficiently accurately. Note that the boundary condition for the streamwise velocity at the domain top is a Neumann type; see Eq. (6). The results at station 1, where the ZPGTBL is expected, agree well with the measurements. The

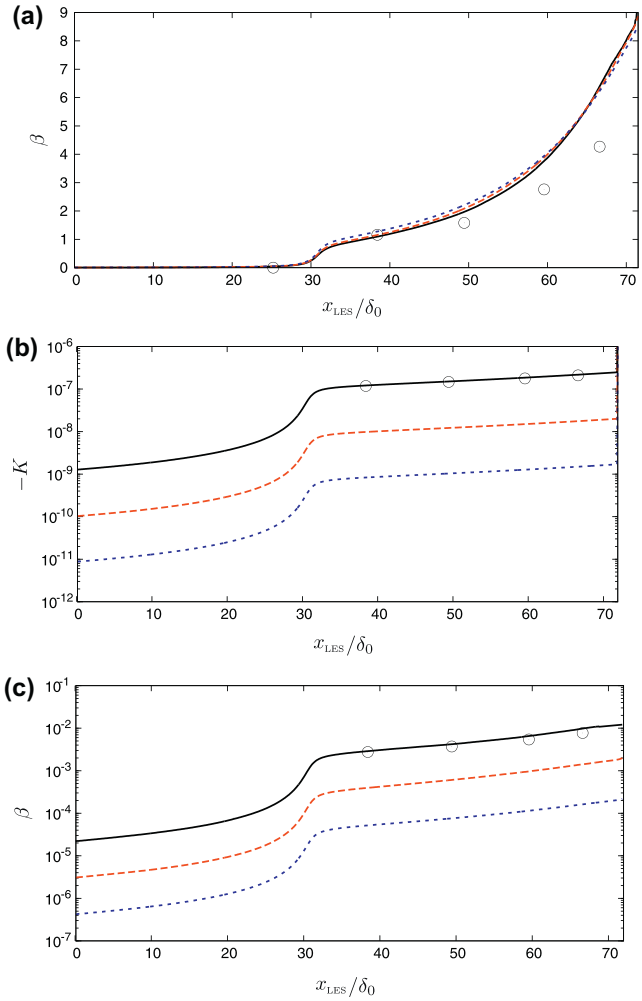

Fig. 4. (a): the pressure gradient parameter β, (b): the acceleration parameter K, and (c): the normalized pressure gradient $(dp/dx)^+ \equiv \nu(dp/dx)/(u_\tau^3)$. Solid; D1, dashed; D4, dotted; D6. ∘: Experimental measurements, see Table 3 for values.

location where the pressure gradient starts to increase is sufficiently downstream from the recycling plane ($x_{\rm ref}$) minimizing the effect of the sudden increase in the pressure gradient on the inflow generation scheme. Along the streamwise direction, however, the results could be interpreted to indicate that the LES is experiencing the effect of adverse-pressure gradient a little more compared to experiments, as shown by a somewhat steeper increase in a pressure gradient parameter β and S.

4.2. Mean velocity profiles

The effect discussed above can be seen in Fig. 5, the mean streamwise velocity $\bar{u}^+ = \bar{u}/u_\tau$ from case D1 normalized by the friction velocity u_τ at five locations along the streamwise direction.

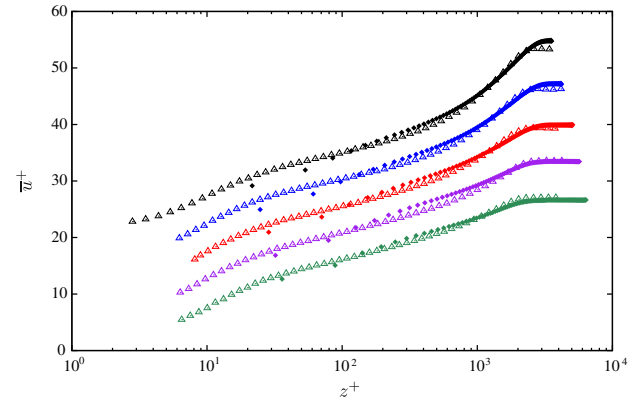

Fig. 5. ◇; case D1 and △; corresponding experimental measurements (Monty et al., 2011) of the mean streamwise velocity. Data are shifted up by 5 units for clarity. From the bottom, station 1 (green), 2 (purple), 3 (red), 4 (blue), and 5 (black). (For interpretation of the references to color in this figure legend, the reader is referred to the web version of this article.)

Reasonable agreement with the measurements was found. Qualitatively, our model reproduces the large wake region which is one of the most recognizable feature of an APGTBL (Clauser, 1954). Similar trends are also found for the higher Reynolds-number cases; see Fig. 6. It should be noted that the amount of amplified wake is somewhat similar at each measurement location irrespective of Reynolds number, which will be discussed in the following section.

Fig. 7 shows the mean velocity defect profiles at five locations from cases D1 to D6 (◇) and experimental results (△). The data are plotted against z/Δ, where $\Delta \equiv \delta^* U_\infty^+$ is the Rotta–Clauser thickness. Data are shifted by 5 units for clarity. From the bottom, station 1 ($\beta \approx 0$), station 2 ($\beta \approx 1.1$), station 3 ($\beta \approx 2.0$), station 4 ($\beta \approx 3.8$), and station 5 ($\beta \approx 6.4$). It is observed that the LES profiles for the flows with Reynolds number ranging from $\mathcal{O}(10^3)$ to $\mathcal{O}(10^5)$ almost coincide in the outer coordinates, indicating good collapse across the outer part of boundary layer. Also the profiles are in good agreement with those of measurements.

Fig. 8(b) shows contour plots of the streamwise velocity, plotted as u/U_∞ and at a time instant during the LES of case D4. Also shown is the ZPGTBL case at the similar Reynolds number in Fig. 8(a). The figures are not in proportion in x and z and each does not display the full domain height in the wall-normal direction. Comparing two plots, a faster development of the boundary layer thickness can be observed. The recycling technique with the use of mirroring method (Jewkes et al., 2011) was removed the spatially quasi-periodic effect that is an inherent feature of the original recycling scheme Lund et al. (1998).

4.3. S-factors

As discussed earlier, it was found that the amount of amplified wake was somewhat similar at each measurement location irrespective of Reynolds number. This can clearly be seen in Fig. 9,

Table 3
Case D1 and corresponding experimental parameters for hot-wire measurements.

	Re_θ		Re_τ		β		$K \times 10^{-7}$		$S = U_\infty/u_\tau$		$dp/dx^+ \times 10^{-3}$	
	Exp	LES	Exp	LES	Exp	LES	Exp	LES	Exp	LES	Exp	LES
1	6560	6540	2330	2410	ZPG	0.04	ZPG	−0.07	27.1	26.8	ZPG	0.13
2	8570	8040	2670	2590	1.16	1.10	−1.18	−1.21	28.5	28.4	2.75	2.93
3	8590	10,100	2380	2770	1.58	1.97	−1.47	−1.51	29.3	29.9	3.71	4.38
4	10,550	12,770	2500	2970	2.76	3.75	−1.78	−1.85	31.2	32.1	5.42	6.82
5	11,630	15,000	2500	2980	4.27	6.41	−2.18	−2.18	33.3	34.7	7.72	9.64

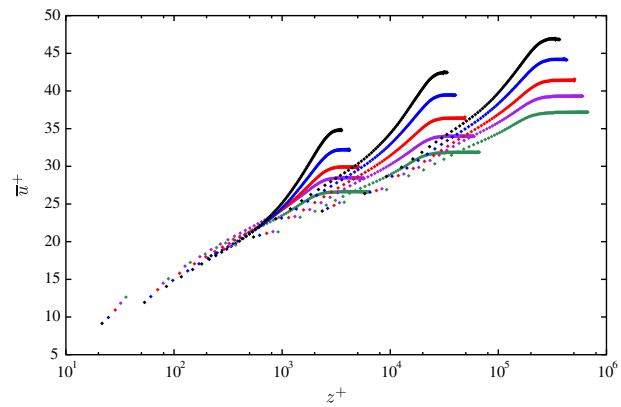

Fig. 6. Mean streamwise velocity from case D1, D4, D6. From the bottom, station 1 (green), 2 (purple), 3 (red), 4 (blue), and 5 (black). (For interpretation of the references to color in this figure legend, the reader is referred to the web version of this article.)

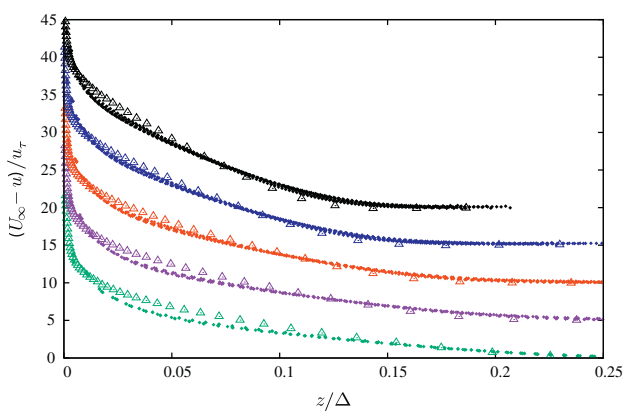

Fig. 7. Mean-velocity defect profiles. ◇; LES. △; experimental measurements. Cases D1 to D6. From the bottom, station 1 (green), 2 (purple), 3 (red), 4 (blue), and 5 (black). For clarity, data are shifted up by 5 units. (For interpretation of the references to color in this figure legend, the reader is referred to the web version of this article.)

showing S values at five locations from cases D1 to D6 with the experimental measurements as a function of the local Re_τ. $S(\beta = 0)$ increases as $\log(Re_\tau)$ as found for the ZPGTBL case (see Inoue and Pullin, 2011). The deviations of S from $S(\beta = 0)$ in each case are shown in Fig. 10. The LES results appear to collapse well at higher Reynolds numbers (case D3–D6). This is well described by the empirical line of best fit

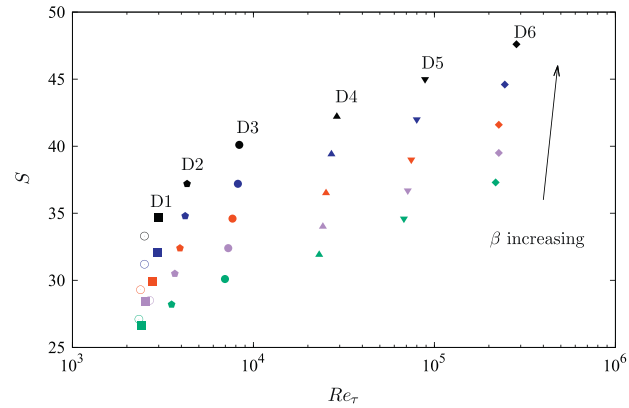

Fig. 9. S-factor as a function of β at five locations from case D1 to D6. From the bottom, station 1 ($\beta \approx 0$), station 2 ($\beta \approx 1.1$), station 3 ($\beta \approx 2.0$), station 4 ($\beta \approx 3.8$), and station5 ($\beta \approx 6.4$) in each case. Open circle: experiment, Harun (2012)

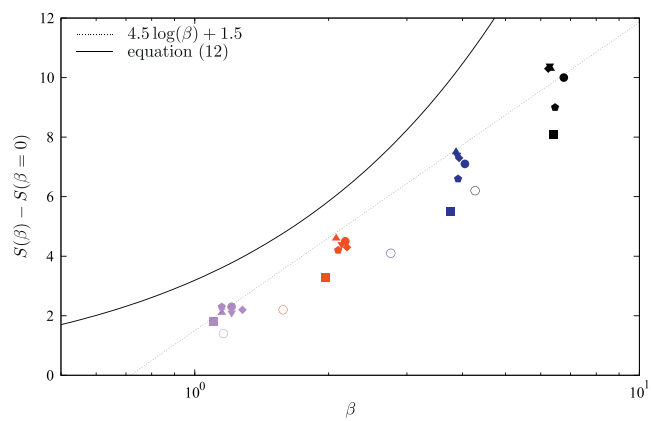

Fig. 10. $S - S(\beta = 0)$ as a function of β. Notation follows Fig. 9.

$$S(Re_\tau, \beta) - S(Re_\tau, 0) = 4.5\log(\beta) + 1.5, \tag{9}$$

which describes our higher Reynolds-number LES. Some transitional behavior is observed from the two lowest Reynolds-number cases D1–D2. It should be noted that the height of the "virtual" wall at station 4 and 5 is below the log region ($h_0^+ = 9.6$ and 8.5 respectively) in case D2. Thus the slip velocity is obtained using Eq. (8) instead of the log-like relationship (Eq. (4b)). The solid line in Fig. 10 is a relation for a flow in "quasi-equilibrium", obtained as follows. Assuming that the mean velocity profile can be described by the Coles (1956) law of the wake Jones et al. (2001) give

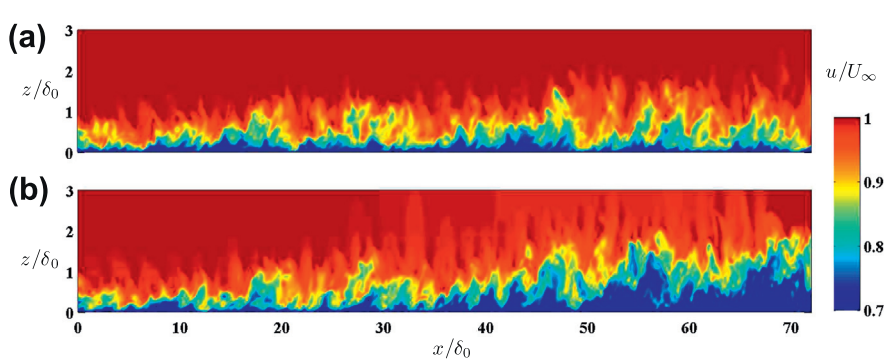

Fig. 8. Contour plot of instantaneous streamwise velocity scaled by the local free-stream velocity, u/U_∞. (a): ZPGTBL with the same Reynolds number as case D4, (b): APGTBL, case D4.

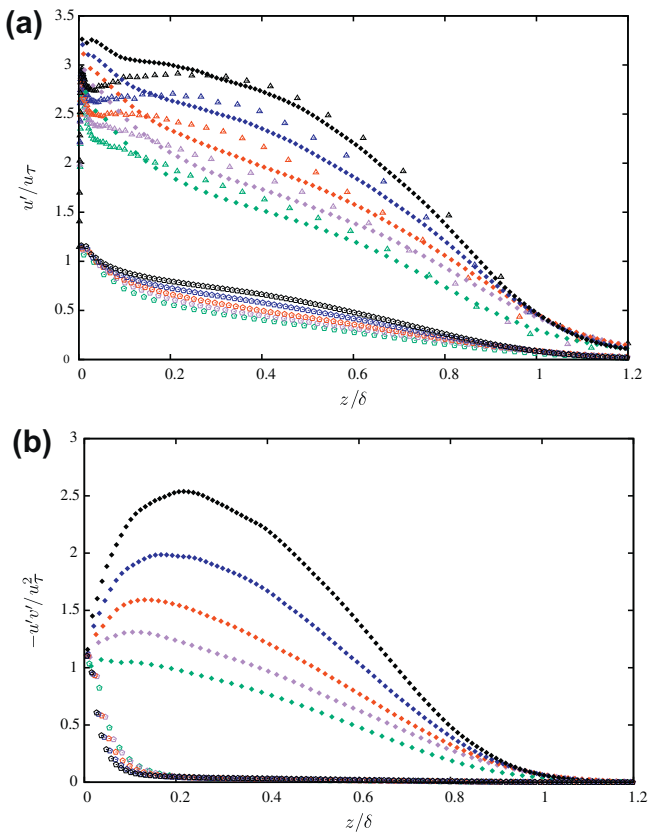

Fig. 11. ◇ solid: LES, open: subgrid contribution, and △; corresponding experimental measurements of (a): streamwise turbulence intensity and (b): Reynolds shear stress from case D1. Station 1 (green), 2 (purple), 3 (red), 4 (blue), and 5 (black). (For interpretation of the references to color in this figure legend, the reader is referred to the web version of this article.)

$$S = U_\infty/u_\tau = \frac{1}{\kappa}\log Re_\tau + A - \frac{1}{3\kappa} + \frac{2\Pi}{\kappa}, \tag{10}$$

where A is the universal smooth-wall constant and κ is the Kármán constant. Here a constant $\kappa = 0.41$ is assumed independent of all other parameters. For a "quasi-equilibrium" flow, defined to be an almost constant wake factor Π, Perry et al. (2002) postulated the following functional relation between Π and β;

$$\beta = -1/2 + 1.21\Pi^{4/3} \quad \text{or} \quad \Pi = 0.86(\beta + 1/2)^{3/4}. \tag{11}$$

Using the second of Eq. (11) in Eq. (10) the deviation of S from $S(\beta = 0)$ can be evaluated as

$$S(\beta) - S(\beta = 0) = \frac{1.72}{\kappa}[(\beta + 1/2)^{3/4} - (1/2)^{3/4}], \tag{12}$$

where $S(\beta = 0)$ corresponds the zero-pressure-gradient case. This relationship is shown in Fig. 10 where it can be seen to be far removed from the present LES and the experimental data. It should be noted that the above discussion is for the APGTBL where the effect of variation in Π along the streamwise direction, represented by a parameter ξ (Perry et al., 2002) can be neglected. The present pressure-gradient distribution appears to produce a nonequilibrium APGTBL.

4.4. Turbulence fluctuation statistics

Another feature of the APGTBL is the increase of turbulence intensity in the outer region when scaled with u_τ, resulting in a second peak, in addition to the peak in the near-wall region (e.g., Marusic and Perry, 1995). Figs. 11 and 12 show the root-mean-square of streamwise velocity fluctuation and the Reynolds shear stress at five locations from LES with the corresponding experimental measurements. No data is available for the Reynolds shear stress. Notations follow Fig. 7. Fig. 11 are from case D1 showing total, resolved plus subgrid contribution, with solid symbols, and subgrid contribution with open symbols. In the outer region, the subgrid contribution to the streamwise velocity fluctuation appears to increase as the flow moves downstream. In other words, the contribution from the scales smaller than the cut-off length Δ_c (defined in the outer length scale) becomes more energetic although most of the increase of the total turbulence intensity is attributed to the resolved scale motions. The SGS model carries most of the Reynolds shear stress only close to the wall. Other cases are not shown since the balance of the resolved and subgrid components is similar.

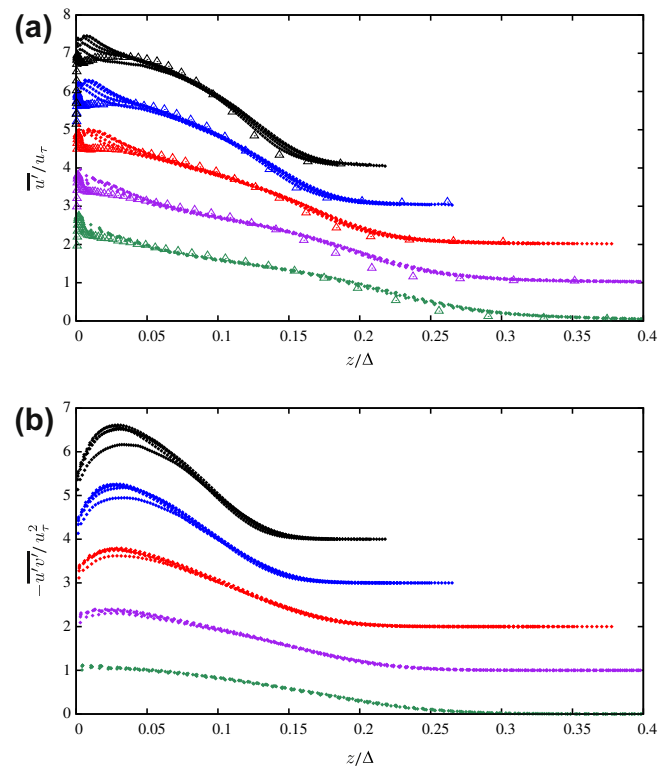

Fig. 12. ◇; LES and △; corresponding experimental measurements of (a): streamwise turbulence intensity and (b): Reynolds shear stress from case D1 to D6. From the bottom, station 1 (green), 2 (purple), 3 (red), 4 (blue), and 5 (black). For clarity, data are shifted up by 1 unit. (For interpretation of the references to color in this figure legend, the reader is referred to the web version of this article.)

The streamwise velocity fluctuation profiles are in good agreement with measurement with small deviations that increase in the region close to the wall owing to the effect of the wall model. This is a limitation of the present wall model. The peak of Reynolds shear stress in the outer region is increasing as β increases when normalized with u_τ and the boundary layer thickness δ. Its location moves away from the wall that is consistent with the previous study, Lee and Sung (2008) for example. The LES appears to reproduce the general changes in the profile shape and the increase in turbulent intensities in the outer region of the boundary layer, corresponding to increases in β in the streamwise direction. But the LES somewhat underestimates the experimental values and does not capture the second peak in the streamwise turbulent intensity at the most downstream station. Fig. 12 are from cases D1 to D6. Data are shifted by 1 unit for clarity. The length scale used for normalization is Δ here. The peak location of Reynolds shear stress seems to be constant. As in Fig. 6 Reynolds number similarity

can be observed in the mean velocity defect, the turbulent intensity and the Reynolds shear stress profiles over two orders of magnitude in Reynolds number when β is held constant.

5. Conclusions

Owing to the local nature of the wall model used, combined with the interior SGS model, the present LES is applicable to the turbulent boundary layers with pressure gradients at both moderate and large Reynolds numbers. The applied pressure gradients reported in the experimental studies (e.g., Harun et al., 2010; Monty et al., 2011) were successfully reproduced in the LES by directly applying pressure as a boundary condition on the upper surface of the computational domain. We first compared results at $Re_\tau \approx 2-3\times10^3$ ($Re_\theta \approx 10^4$) with experimental measurements using a relatively long domain, $L_x = 72\delta_0$. Except for the region close to the wall, the mean velocity profiles and turbulent intensity were found to be in reasonable agreement with experiments, including the pressure gradient parameters, β, K, and $(dp/dx)^+$. The recognizable features of the APGTBL, such as an amplified wake in the mean velocity profile and an increase in turbulent intensity in the outer region were reproduced. Most importantly, it was found that our wall ODE was capable of simulating the correct distribution of the wall shear stress along the streamwise direction under an adverse-pressure gradient.

We also performed LES of the "nonequilibrium" APGTBL, by the definition of Perry et al. (2002), at Reynolds number up to $Re_\tau \approx 2\times10^5$ ($Re_\theta \approx 10^6$) using the same profile of pressure-gradient distribution, so that the flow experienced the same upstream history of the pressure gradient. The resulting distribution of β was found not to be very sensitive to the Reynolds number itself and showed similar profiles for the various LES performed. The mean velocity defect and the turbulent intensity profiles, when normalized by the friction velocity u_τ and Rotta–Clauser parameter Δ, shows good collapse in the outer part of boundary layer over a wide range of Reynolds number at each measurement station, where almost matched β is achieved. Harun et al. (2010) has reported the similar behavior although over a smaller range of Reynolds number. The present LES demonstrates that use of a wall model that specifically incorporates local pressure gradients enables successful LES of nonequilibrium, developing boundary-layer flows.

Acknowledgement

This work has been supported in part by the National Science Foundation under Grant CBET-1235605. DIP also acknowledges travel support of the Australian Research Council.

References

Bradshaw, P., 1967. The turbulence structure of equilibrium boundary layers. Journal of Fluid Mechanics 29 (04), 625–645.
Chung, D., Pullin, D., 2009. Large-eddy simulation and wall-modeling of turbulent channel flow. Journal of Fluid Mechanics 631, 281–309.
Clauser, F.H., 1954. Turbulent boundary layers in adverse pressure gradients. Journal of the Aeronautical Sciences 21, 91–108.
Clauser, F., 1956. The turbulent boundary layer. Advances in Applied Mechanics 4 (1).
Coles, D., 1956. The law of the wake in the turbulent boundary layer. Journal of Fluid Mechanics 1 (2), 191–226.
Gottlieb, D., Shu, C., 1997. On the Gibbs phenomenon and its resolution. SIAM Review 39 (4), 644–668.
Harun, Z., 2012. The Structure of Adverse and Favourable Pressure Gradient Turbulent Boundary Layers. Ph.D. Thesis, The University of Melbourne, Melbourne.
Harun, Z., Monty, J., Marusic, I., 2010. Constant adverse pressure gradient turbulent boundary layers. In: 17th Australian Fluid Mechanics Conference, Auckland, New Zealand.
Henkes, R., Skote, M., Henningson, D., 1997. Application of turbulence models to equilibrium boundary layers under adverse pressure gradient. In: 11th Symposium on Turbulent Shear Flows, Grenoble, France. pp. 33–13.
Hickel, S., Adams, N., 2008. Implicit les applied to zero-pressure-gradient and adverse-pressure-gradient boundary-layer turbulence. International Journal of Heat and Fluid Flow 29 (3), 626–639.
Inoue, M., Pullin, D., 2011. Large-eddy simulation of the zero pressure gradient turbulent boundary layer up to $Re_\theta = O(10^{12})$. Journal of Fluid Mechanics 686, 507–533.
Jewkes, J., Chung, Y., Carpenter, P., 2011. Modification to a turbulent inflow generation method for boundary-layer flows. AIAA Journal 49 (1), 247–250.
Jones, M., Marusic, I., Perry, A., 2001. Evolution and structure of sink-flow turbulent boundary layers. Journal of Fluid Mechanics 428, 1–27.
Lee, J., Sung, H., 2008. Effects of an adverse pressure gradient on a turbulent boundary layer. International Journal of Heat and Fluid Flow 29 (3), 568–578.
Lee, J., Lee, J., Lee, J., Sung, H., 2010. Coherent structures in turbulent boundary layers with adverse pressure gradients. Journal of Turbulence 11 (28), 1–20.
Lund, T., Wu, X., Squires, K., 1998. Generation of turbulent inflow data for spatially-developing boundary layer simulations. Journal of Computational Physics 140 (2), 233–258.
Marusic, I., Perry, A., 1995. A wall-wake model for the turbulence structure of boundary layers. Part 2. Further experimental support.. Journal of Fluid Mechanics 298, 389–407.
Mellor, G., Gibson, D., 1966. Equilibrium turbulent boundary layers. Journal of Fluid Mechanics 24 (2), 225–253.
Monty, J., Harun, Z., Marusic, I., 2011. A parametric study of adverse pressure gradient turbulent boundary layers. International Journal of Heat and Fluid Flow 32 (3), 575–585.
Morinishi, Y., Lund, T., Vasilyev, O., Moin, P., 1998. Fully conservative higher order finite difference schemes for incompressible flow. Journal of Computational Physics 143 (1), 90–124.
Nagano, Y., Tsuji, T., Houra, T., 1998. Structure of turbulent boundary layer subjected to adverse pressure gradient. International Journal of Heat and Fluid Flow 19 (5), 563–572.
Nagib, H.M., Chauhan, K.A., 2008. Variations of von Kármán coefficient in canonical flows. Physics of Fluids 20, 10151801–10151810.
Nickels, T., 2004. Inner scaling for wall-bounded flows subject to large pressure gradients. Journal of Fluid Mechanics 521 (1), 217–239.
Perot, J., 1993. An analysis of the fractional step method. Journal of Computational Physics 108 (1), 51–58.
Perry, A., Marusic, I., 1995. A wall-wake model for the turbulence structure of boundary layers. Part 1. Extension of the attached eddy hypothesis. Journal of Fluid Mechanics 298, 361–388.
Perry, A., Marusic, I., Li, J., 1994. Wall turbulence closure based on classical similarity laws and the attached eddy hypothesis. Physics of Fluids 6 (2), 1024–1035.
Perry, A., Marusic, I., Jones, M., 2002. On the streamwise evolution of turbulent boundary layers in arbitrary pressure gradients. Journal of Fluid Mechanics 461, 61–91.
Schofield, W., 1981. Equilibrium boundary layers in moderate to strong adverse pressure gradients. Journal of Fluid Mechanics 113, 91–122.
Simens, M., 2008. The Study and Control of Wall-bounded Flows. Ph.D. Thesis, Aeronautics, Universidad Politécnica, Madrid, Spain. <http://oa.upm.es/1047>.
Skåre, P., Krogstad, P., 1994. A turbulent equilibrium boundary layer near separation. Journal of Fluid Mechanics 272 (1), 319–348.
Skote, M., Henningson, D., Henkes, R., 1998. Direct numerical simulation of self-similar turbulent boundary layers in adverse pressure gradients. Flow, Turbulence and Combustion 60 (1), 47–85.
Spalart, P., Moser, R., Rogers, M., 1991. Spectral methods for the Navier–Stokes equations with one infinite and two periodic directions. Journal of Computational Physics 96 (2), 297–324.
Wu, X., Moin, P., 2009. Direct numerical simulation of turbulence in a nominally zero-pressure-gradient flat-plate boundary layer. Journal of Fluid Mechanics 630, 5–41.